2020 American Control Conference
Denver, CO, USA, July 1-3, 2020

An experimental study on process modeling for selective laser melting*

Aleksandr Shkoruta[1], Sandipan Mishra[1] and Stephen Rock[2]

***Abstract*— This paper addresses process modeling for the selective laser melting (SLM) process. We experimentally investigate the response of the SLM process output (measured by a coaxial near-infrared camera) to changing input laser power. We determined that first and second order models can be used to capture this input-output behavior. Next, we studied the dependency of this transfer function on laser scan speed and other process variables that evolve over a typical part build, such as thermal properties of surrounding medium (bulk powder, build plate, or solidified part) or layer number. The transfer function was found to strongly depend on the material environment (solidified material or bulk powder). Further, transfer function also depended on the layer number, exhibiting transient behavior. We report identified 1st order transfer functions for different scan speeds, locations on the build plate, and different layer numbers. Identified models and quantification of their variability will serve as foundational work for the future implementation of advanced real-time process control algorithms.**

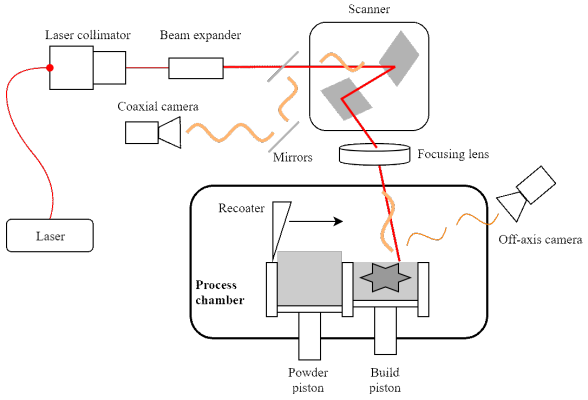

Fig. 1. Schematic of the L-PBF (SLM) process.

I. INTRODUCTION

Additive manufacturing (AM) is a set of processes that produce parts by adding, not subtracting, material. There are at least 7 distinct families of such processes, "powder bed fusion" (PBF) being one of them [1]. In laser PBF (L-PBF), also known as selective laser melting (SLM), bulk material in the form of the powder is contained within the process chamber with a controlled atmosphere and is supported by a vertically traveling platform. A tightly focused high-power laser scans the powder surface according to the part geometry, selectively melting the material, as shown in Figure 1. Upon completion of the scan, the build platform lowers, and a new layer of powder is deposited on top of the freshly scanned surface. This way, a part is created in a layer by layer fashion.

Thermal effects inherent to SLM (high cooling rates, non-uniform heating, and temperature cycling) are known to produce defects: porosity, deformation, and cracking [2]. It is universally agreed upon that to achieve better final part quality, in-situ real-time control is necessary. However, as of now, process control of SLM is lacking, mainly due to (1) challenges in real-time temperature measurement and (2) lack of control-oriented process models [3].

SLM presents significant challenges for real-time measurement. The melt pool is small and its dynamics are fast, requiring high spatial (on order of 10 microns per pixel) and temporal (on order of 10 kHz) sensor resolution. However, such demands are challenging even for state-of-the-art temperature monitoring instrumentation.

The lack of control-oriented process models in SLM is a well-documented challenge [3]. Existing SLM process models are computationally intensive and not suitable for real-time process control. A variety of different control strategies have been reported for other laser AM processes (for example, [5]). For SLM, however, only a PI controller based on photodiode measurements has been experimentally demonstrated [6], [7]. Recently, feedforward strategies such as iterative learning control [8] have shown promise for optimizing laser power profiles for specific scan patterns.

In this work, we sought to establish transfer function models linking the laser power input with the available melt pool emission measurements. We have also investigated the potential dependence of such models on the process stage (i.e. layer number) and the surrounding material properties. We found strong differences between transfer functions for solid material and powder. Transfer functions also behaved differently with respect to scan speed. We also observed transient behavior of the transfer function in the initial layers of the build.

The paper is structured as follows: we state the modeling and control problem and introduce process nomenclature in Section II. Then, we review the experimental setup (open-source SLM testbed) in Section III. Section IV describes the approach to model identification. Experiments performed are discussed in Section V. Model identification results are presented and discussed in Section VI.

*This work is supported by NSF Data-Driven Cyberphysical Systems Award #1645648 and by the State of New York ESD/NYSTAR program.

[1] Aleksandr Shkoruta and Sandipan Mishra are with Department of Mechanical, Aerospace, and Nuclear Engineering, Rensselaer Polytechnic Institute, Troy, NY 12180, USA. shkora,mishrs2@rpi.edu

[2] Stephen Rock is with Center for Automation Technologies and Systems, Rensselaer Polytechnic Institute, Troy, NY 12180, USA. rocks@rpi.edu

II. PROBLEM STATEMENT

Consider a laser scanning the build area. Let $\{t_i, i = 1, 2, \ldots\}$ be discrete time instants and denote laser power input at t_i as $p(t_i)$. Let $I(t_i) \in \mathbb{R}^n$ be a (multi-dimensional) process output, and denote its reduced 1D signature as $M(t_i) = \mathcal{F}(I(t_i))$, $\mathcal{F} : \mathbb{R}^n \to \mathbb{R}$. For example, I could be an intensity image, and M be an image statistic, e.g. mean. We seek to identify a suitable transfer function $G(s)$ from the laser power input $P(s)$ to the output signature $M(s)$ from the experimentally collected input-output data.

In this paper, we identify first and second order transfer function models of the form:

$$G(s) = \frac{K}{\tau s + 1} \equiv \frac{K/\tau}{s + \omega_c}, \quad G(s) = \frac{K\omega_n^2}{s^2 + 2\zeta\omega_n s + \omega_n^2}$$

where all symbols have their commonly accepted interpretation. Further, we investigate the effect of various process parameters (e.g. scan speed) on these identified transfer functions and discuss the variability caused by these changing process parameters.

III. OPEN-SOURCE SLM TESTBED

In this section, we describe the hardware used to obtain the control-oriented process models. The process modeling experiments were conducted on an open-source SLM testbed that was built in-house at Rensselaer Polytechnic Institute. The testbed adheres to the conventional SLM machine architecture, where an Nd-YAG laser beam is redirected by two rotating mirrors of a servo-controlled scanner. Subsequently, the laser is focused onto the build area by a flat-field lens. This testbed is constructed with an open architecture that enables full synchronized access to all motor input signals, scanner and laser control command signals and all process parameters (for example layer thickness, hatch spacing, or scan speed) in real time. The testbed has two cameras for in-process measurement and feedback: a larger field-of-view (FOV) thermal camera in a staring configuration ("off-axis"), and a smaller FOV near-infrared (NIR) camera for the melt pool area observation ("coaxial"), as shown in Figure 1. The machine operation is controlled from an industrial PC. Large parts of the process control code were implemented in LabVIEW and are courtesy of America Makes [9], while the coaxial camera image acquisition and the dynamic power control codes are written in-house in C++. The full equipment list is presented in Table I.

TABLE I
EQUIPMENT LIST

Laser	IPG Photonics 1070 nm $40 - 400$ W power range
Beam expander	Sill Optics S6EZM5076/328 motorized, up to $8\times$ magnification
Scanner	SCANLAB intelli*SCAN*$_{de}$ 20 typical marking speed 1 m/s step response (1% full scale) 0.7 ms
Focusing lens	Sill Optics S4LFT1420 focal length 420 mm nominal spot $\varnothing 60$ μm ($\varnothing 14$ mm beam)
Off-axis imaging	FLIR A320 waveband $7.5 - 13$ μm $320 \times 240,\ 60$ Hz
Coaxial imaging	Basler acA2000-165umNIR filter waveband $800 - 950$ nm 32×32 subwindow, 3500 Hz
Scanner controller	SCANLAB RTC5 PCI control board
Main PC	General Electric RXi-XP Industrial PC 2.5 GHz CPU, 8 GB RAM, Windows 7
Motion controller	Galil DMC-4080

In this work, we use real-time measurements from the coaxial NIR camera as the output signal to find the transfer functions (TFs) associated with the SLM process. Process emissions from the melt pool area (orange waves in Figure 1) reflect back through the scanner mirrors and impinge on a beam-splitter (in gray at $45°$ to laser line), which is transparent for the laser radiation (shown in red) but reflects shorter wavelengths. Then, these process emissions can be imaged by the NIR camera. Such a setup is widely employed, with most recent installments reported in [10], [11].

Coaxial NIR monitoring has several advantages. First, the camera's FOV is always aligned with the laser location thanks to the scanner mirrors. As such, the melt pool is always centered in the image, and the camera frame can be cropped (sub-windowed), which allows for higher frame rates. Second, as the imaging wavelengths are shorter than 1 micron, inexpensive Si-based detector-based camera can be used, which also allows for higher frame rates.

The coaxial camera operates in a hardware triggered mode. An image is transmitted via USB3 cable to the industrial PC (running under Windows OS), where the image is saved for the later analysis. We empirically evaluated resultant sample time to be $290\,\mu s$, e.g. 3448 Hz sampling frequency (for a nominal 3500 Hz setting).

The laser power is controlled from a real-time PCI controller board, which is plugged into the same industrial PC and is driven by a LabVIEW program. Therefore, synchronized power control capabilities are at 1 kHz update rate, as determined by the internal Windows/LabVIEW timer (1 ms interval). The synchronization of the image acquisition (*on the PC*) and power update command is compromised by non-real-time OS. However, we command laser power and acquire camera frames (*on the camera*) with consistent frequencies. As such, acquired data and the power signal are repeatable and synchronized, once they are aligned off-line, which compensates for non-real-time jitter of the scan start time.

The camera has an internal buffer storage of a programmable size (currently set to 5 frames), which eliminates the frame dropout but also introduces delays into the measurement setup. Empirically, a combination of the current buffer size and non-deterministic Windows scheduler-related delays appears to result in the acceptable system performance.

A typical image acquired by the coaxial camera during the

SLM process is shown in Figure 2a. At 3500 fps, a simple rectangular part ($30 \times 10 \times 1\ mm^3$) generates 2 GB of data, necessitating some form of data reduction. In this work, we use the average intensity (mean digital level) M of the entire image as the process signature (which has strong correlation to the melt pool size):

$$M(t) = \frac{1}{RC} \sum_{r,c} I(r, c, t)$$

where $r \in \{1 \dots R\}, c \in \{1 \dots C\}$ are the row and column indices within a single image, t is the time of an image acquisition, and $I(r, c, t)$ is the intensity of the pixel at the position r, c in the frame acquired at t.

In the next sections, we present the methodology for identification of the process TFs, as well as investigation of the dependence of these functions on various evolving process parameters.

IV. IDENTIFICATION METHODOLOGY

We identified TF models from input-output data obtained in a set of single line scan experiments. For each line, we commanded a time-varying input power profile and collected corresponding coaxial images. The input power profile was generated in MATLAB using pseudo-Gaussian mode of `idinput` function. An example of the acquired data is shown in Figure 3. For each line, we fit a TF model using MATLAB's System Identification Toolbox. First, we synchronized the camera measurement and power commands in time. Then, the mean values were subtracted from data to remove DC-bias, and several candidate TF models were identified using MATLAB's `tfest`. A detailed discussion of the model order selection is presented in Section VI-A below. The quality of the fit was measured by normalized root mean square error:

$$fit = \left(1 - \frac{||M - \hat{M}||_2}{||M - \overline{M}||_2}\right) \times 100\%$$

where $M \in \mathbb{R}^n$ is the measured output, $\overline{M}$ is the mean value of the measured output, and $\hat{M} \in \mathbb{R}^n$ is the identified model output.

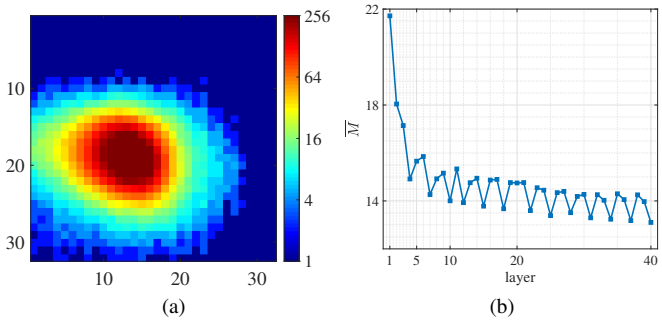

Fig. 2. (a) Example coaxial image. Note the logarithmic scale of intensity. (b) Mean layer signature $\overline{M}$ decreases with layer number. Observable oscillations are due to the changing scan pattern (two scans are diagonal and one is lateral). Values that fall out of order are explained by the build process interruption for the single line runs, see the description of Experiment D.

V. EXPERIMENT DESIGN

The process response (i.e., melt pool emissions measured by the NIR camera) to laser power input will necessarily depend on the laser scan speed but may also vary with the (1) location on the build plate (due to location-dependent proximity to solid metal chamber walls) or (2) the type of surrounding medium: if the current location rests on the solid build plate, previously built-up part, or bulk powder. Furthermore, (3) height of the built-up part e.g. number of layers might also play a role.

The first two sources of variation are the result of significantly different thermal properties of bulk powder and bulk solid metal. Due to the lower thermal conductivity of the surroundings, locations that are completely surrounded by powder accumulate heat. On the other hand, if a location is close to a solid metal region, that metal acts as a heat sink. Thus, it is reasonable to expect that coaxial signature's behavior might depend on the surrounding material.

The effect of layer number requires further elaboration. Our prior studies [12] have noted that coaxial signatures often show decreasing trends with increasing layer number. This effect is further underscored by the data acquired during this study. In Figure 2b, the mean value of signature M for the *whole layer* is plotted against layer number. It can be clearly seen that the process signature evolves as layers are built, ultimately settling into a steady state behavior after 10-20 layers. Thus, it is of interest to evaluate how experimentally identified process model changes from layer to layer.

To select the TF model structure and to investigate potential dependence of identified TFs on scan speed, build plane location, material state, and layer number, we performed the following sets of experiments:

A: The same line (20 mm, scan speed 300 mm/s) was scanned over the bare solid plate four times. A spatial separation between these 4 repetitions was kept at 1 mm

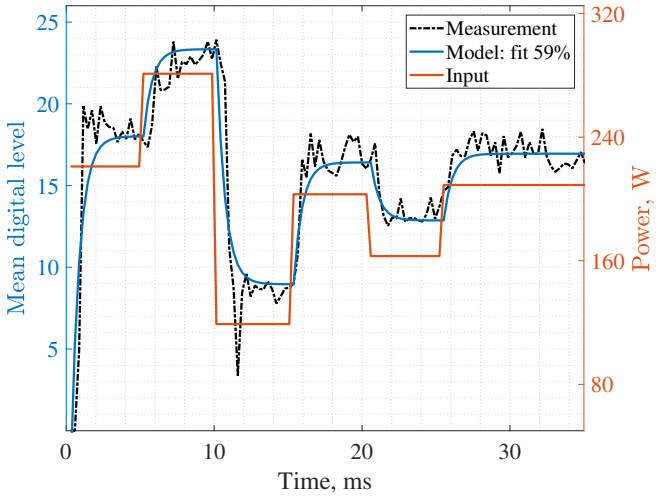

Fig. 3. Example input power profile, corresponding output, and model fit. The measurement data is noisy, thus fit values of 50-60% are considered 'acceptable'.

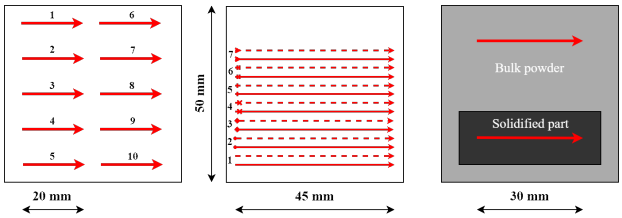

Fig. 4. (a) Experiment B: laser-scanned lines are shown in red, with the direction of the scan indicated by arrows. (b) Experiment C: 7 pairs of lines correspond to 7 different scan speeds. Solid line from each pair was used for identification, while dashed line was used for validation. (c) Experiment D: part-supported and powder-supported lines evolving with layer number. Powder is shown in light gray and built-up part is in dark gray.

to limit the effects of spatial location on the results.

B: 10 instances of the same line (20 mm, scan speed 600 mm/s) were scanned in different locations on the build plate. In one case, we used bare solid plate, and in the other, lines were scanned over deep powder bed[1] (Figure 4a).

C: 7 pairs of long (45 mm) lines were scanned over both solid plate and deep powder bed. Following scan speeds were used: 200, 400, 600, 800, 1000, 1200, and 1400 mm/s (Figure 4b).

D: A simple prismatic SLM part was built with 40 layers total[2]. For layers 1, 2, 5, 10, 20 and 40, we paused the process and scanned two lines: a single line over the deep powder area and a single line over the built-up part (Figure 4c).

Experiments A and B allowed us to select the model structure, evaluate model uncertainty, and study the model dependence on the build plane location. Influence of scan speed on identified TF parameters was evaluated based on the results of Experiment C. Finally, input-output data for different depths of underlying powder and SLM-produced substrates from Experiment D provided insight into evolution of identified TF models with layer number and their dependence on underlying material.

VI. RESULTS

A. Model order selection

To determine the appropriate model order, we used input-output data from first 3 lines from Experiment A for model identification and retained the last one for validation purposes. From prior literature [6] and simplified heat-transfer models [13], it is expected that the model should be of 1st or 2nd order. Therefore, we identified TFs with (1) a single pole (1P) and (2) two poles, with and without a zero (2P1Z and 2P, correspondingly). The 2P1Z models showed pole-zero cancellations, which indicated a poor choice of model

[1]We ensured that more than 2 mm of CoCr powder separated the top surface from the solid substrate of the build platform in any of the "deep powder" tests.

[2]250 W, 600 mm/s nominal parameters; $45°$, $-45°$, and $0°$ layer scan orientations. Layer thickness is $30\,\mu m$.

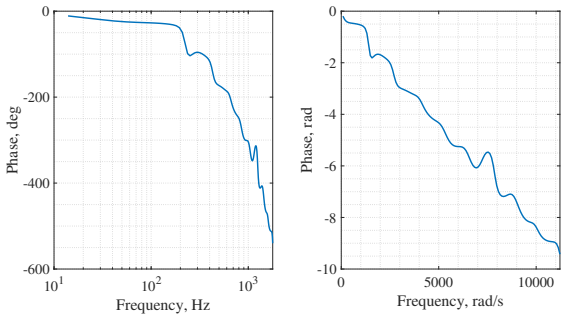

Fig. 5. Phase of frequency response drops drastically. Linear trend (on the right) w.r.t. frequency indicates constant delay, which is $825\ \mu s$ (based on the slope) in this case.

structure and over-parameterization[3].

Delays are expected from the camera image acquisition process, which is further supported by the Bode phase plot (Figure 5), where the presence of a constant delay is evident. Thus, we have also identified 1P and 2P models with delays (1PD and 2PD).

A comparison of these identified models' outputs is shown in Figure 6. It is evident that introduction of the delay did not significantly improve the corresponding 1P and 2P models, thus delayed models are omitted from now on.

For the identified model parameters, we refer the reader to Tables A.1 (1st order) and A.2 (2nd order) in the Appendix.

1P and 2P models had quantitatively similar fits. From a simplicity standpoint, the 1st order model is superior. However, an overshoot was sometimes observed in the output response when laser power increased. Interestingly, corresponding output overshoot when power *decreases* is rarely seen, as evident from Figure 7. Therefore, we were left with a choice between (a) 1st order model that did not capture this effect at all or (b) 2nd order model that predicted

[3]This is further supported by the TF identification on the data from latter Experiments B, C.

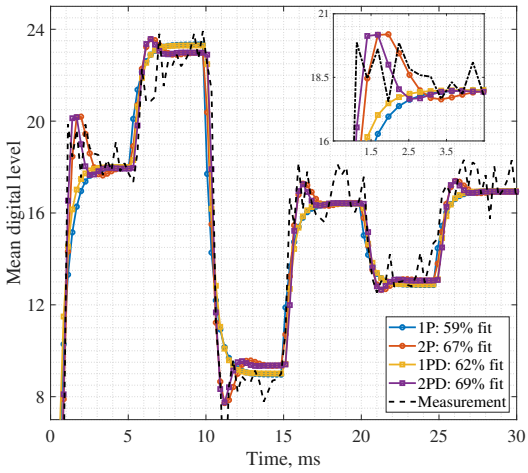

Fig. 6. Model order selection. Non-delayed and delayed TFs are almost identical. However, there is an observable difference between identified 1st and 2nd order models. Inset at the top right corner shows zoomed-in response to the first step power change.

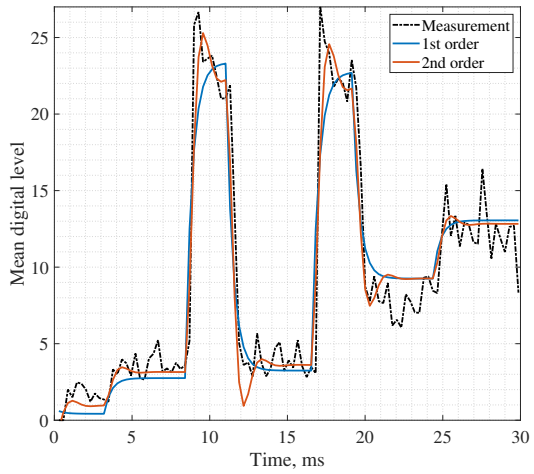

Fig. 7. Characteristic example of the output behavior: large overshooting spikes with step-wise increase in laser power, monotonic decrease with the laser power drop. Data: Experiment B, solid plate. Qualitatively similar behavior is also observed in deep powder tests.

spurious overshoot when power dropped. We thus proceeded with *the 1st order TF because it was simpler while providing a fit comparable with 2nd order TF*. However, overshoot and undershoot in step response to laser power change should be investigated further.

It is important to stress the high variability of the output signal, even when laser power input is held constant[4]. This issue is more prevalent in tests with powder than with solid metal plate due to the discrete powder particles' effects e.g. spatter.

B. Effect of the location on the build plate

One potential source of the variability in the identified TF is the location on the build plate (in the XY plane, with Z being vertical direction). If the location on the build plate does indeed affect the process response significantly, one can expect the TFs identified from the outer lines (1, 5, 6 and 10 in Figure 4a) to systematically differ from the inner ones (2-4, 7-9).

[4]Standard deviation depends on process parameters and is generally in the 0.8 - 1.8 range, with lowest values corresponding to lower energy densities and solid material substrate.

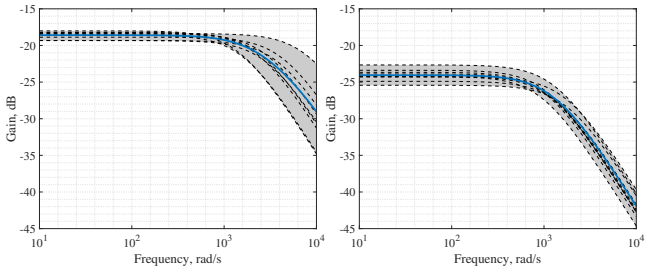

Fig. 8. Bode magnitude plot for the 1st order TFs identified in Experiment B, for solid plate (a) and deep powder (b).

We used data acquired from Experiment B (both on solid plate, and in deep powder) to identify 1st order TF for each scan line[5]. Identified model parameters did not exhibit any obvious trends or particular consistent spatial patterns, in both solid plate and deep powder cases. *Based on this, we believe that spatial location on the build area has at best a marginal influence on the process TF.* Superimposed Bode magnitude plots for all identified 1st order TFs are shown in Figure 8. Identified parameters are listed in Tables B.1, B.2 in Appendix.

C. Effect of the laser scan speed

After laser power, laser scan speed is arguably the second most important process parameter in SLM and its influence on the identified TFs is of particular interest for any laser power control design strategy. In Experiment C, wide range of speeds was tested both on solid plate and in deep powder, which allowed us to evaluate the influence of speed on identified TF parameters. We used the first line in each pair for model identification and validated resulting model on the input-output data from the second line in a pair.

Figure 9 shows dependence of identified gains and time constants on scan speed. Interestingly, gains for deep powder and solid plate cases exhibit opposite trends: *the gain (in dB) for solid plate linearly decreases with increasing scan speed while the gain for deep powder slightly increases with*

[5]We used the results from the previous subsection (averaged model) as an initial guess for the identification algorithm.

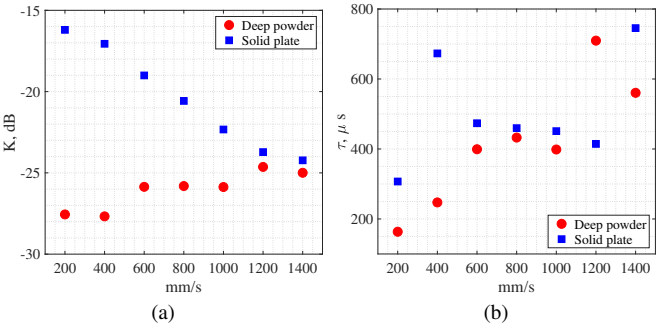

Fig. 9. (a) Dependence of the gain on the scanning speed. (b) Dependence of the time constant on the scan speed.

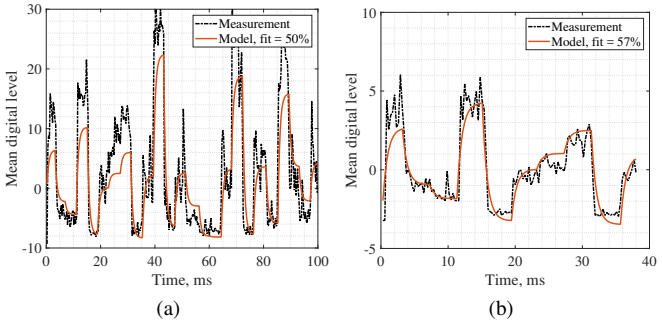

Fig. 10. Fits of the identified 1st order TFs: (a) solid plate, 400 mm/s (b) deep powder, 1200 mm/s.

scan speed. The time constants exhibit some variability but seem to generally increase with scan speed. Viewed in spatial domain, this effect persists i.e. this trend is not due to the increased distance travelled per acquired sample. Figure 10 shows two of the identified models (solid plate 400 mm/s on the left and deep powder 1200 mm/s on the right) that are particularly out of trend. Their quality of fit does not seem to explain scatter of time constants.

Results are presented in Tables C.1 (solid plate) and C.2 (deep powder) in Appendix.

D. Effect of the supporting material and layer number

From previous sections it is clear that process output (measured by the coaxial camera) behaves differently depending if bulk powder or solid plate are scanned. In the actual SLM process, scans typically occur over the part-supported or powder-supported areas. In the former, SLM-produced surface lays directly underneath current line scan. In the latter, there is only powder under the laser. For SLM process control, both of these modes are of interest. Using data from Experiment D, we identified 1st order TF models for part- and powder-supported output data, for different layer numbers.

Powder-supported and part-supported TF are initially overlapping, as is evident from the Bode magnitude plots (Figure 11). This is understandable, as one or two layers of powder do not prevent melt pool from penetrating all the way down to the solid build plate. *There is clearly a transient behavior, as TFs take around 5-10 layers to settle and achieve steady shapes*. In the end, powder-supported and part-supported TF are clearly separated by 4 dB.

Figure 12 shows evolution of the identified model parameters with layer number. In both powder- and part-supported cases, gains are clearly decreasing as the part builds up and depth of the powder bed grows (Figure 12a). All identified model parameters are listed in Table D in Appendix.

Remark. 40 layers of powder amount to 1.2 mm of total powder thickness, thus the powder-supported TF identified at layer 40 should have been similar to the ones identified in previous deep powder tests (namely, Experiments B and C). However, there is observable difference in gain values (-25 dB for Experiment B and -28 dB for Experiment D). As those were different tests (different powder recoating, for example), there are many possible reasons for such a discrepancy, i.e. potential residual heat accumulation. Indeed, in Experiment D laser scanning was occurring for the prolonged period of time, and total energy input is large. On the contrary, total amount of energy emitted by laser is negligible in the single line tests. The discrepancy between identified deep powder gains is currently under investigation.

VII. CONCLUSION

In this paper, we have identified TF models from the laser power input to coaxial signature of the melt pool emissions in SLM. Output data appears to have high variation, which could be explained by the influence of discrete powder particles' effects on the process emission. We have established

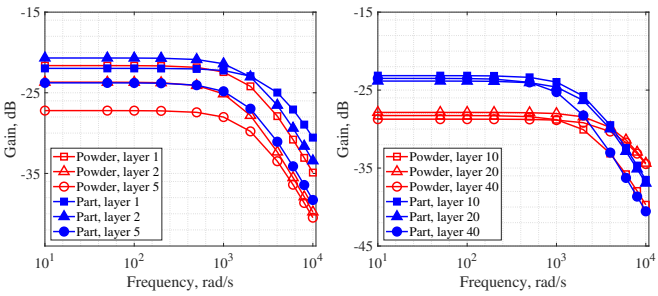

Fig. 11. (a) Identified TFs change with layer number for the first several layers. (b) After the initial transient, TFs seem to settle.

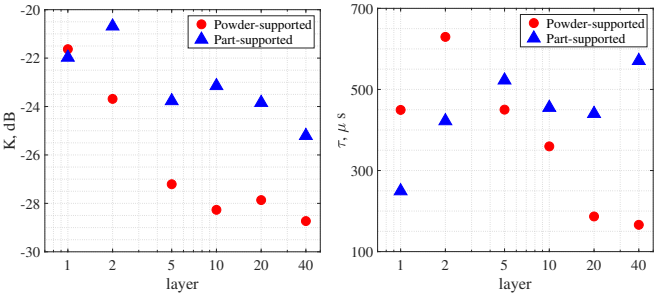

Fig. 12. Dependence of (a) gain and (b) time constant on layer number, powder- and part-supported cases.

that 1st order TF models are the preferable model structure, given the nature of input-output data and achievable fits. Identified TFs clearly and predictably depend on laser scan speed and material state (solid plate, SLM-produced part, or bulk powder). We have also shown that TF do not achieve consistent shapes instantly but exhibit transient behavior during layer build-up, i.e. for the first 5 - 10 layers of a build TFs are settling into steady-state. This work provides the necessary background information on SLM process outputs for the ongoing work in implementation of the advanced real-time data-based control strategies in SLM.

APPENDIX

We acquired "merged" models using MATLAB's `merge` command, while "averaged" used averaged model parameters. Validation process was the same as for 3 original models. Asterisk (e.g. #5*) denotes an outlier. Mean and standard deviation are calculated based on data with outliers excluded.

TABLE A.1
1ST ORDER MODELS, SOLID PLATE

Line	K, dB	τ, μs	ω_c, rad/s	fit, %	validation %
#1	-21.481	476	2099.2	75	63.4
#2	-21.037	563	1776.6	59	63.4
#3	-21.606	631	1583.8	52	63.6
Merged	-21.556	704	1421.2		63.2
Averaged	-21.374	557	1795.7		63.3

TABLE A.2

2ND ORDER MODELS, SOLID PLATE

Line	K, dB	ζ	ω_n, rad/s	fit, %	val, %
#1	-21.559	0.480	2690.9	76	67.3
#2	-21.522	0.553	2540.4	67	67.4
#3	-21.820	0.671	2229.7	62	66.8
Merged	-22.345	0.452	1853.3		67.1
Averaged	-21.634	0.568	2487.0		56.4

TABLE B.1

1ST ORDER MODELS: INFLUENCE OF LOCATION, SOLID PLATE

Line	K, dB	τ, μs	ω_c, rad/s	fit, %
#1	-18.002	684.9	1460.0	64
#2	-18.874	226.7	4410.5	74
#3	-18.220	438.6	2279.8	65
#4	-18.380	126.2	7923.2	70
#5*	-19.205	28.5	35131.3	68
#6	-19.316	257.6	3882.5	58
#7	-19.332	344.7	2901.5	66
#8	-18.589	622.1	1607.5	59
#9	-18.249	406.5	2459.9	66
#10	-18.438	337.3	2964.8	56
	-18.60 $\pm$0.45	383 $\pm$170	3321 $\pm$1862	

TABLE B.2

1ST ORDER MODELS: INFLUENCE OF LOCATION, DEEP POWDER

Line	K, dB	τ, μs	ω_c, rad/s	fit, %
#1	-23.867	876.2	1141.3	60
#2	-24.094	816.8	1224.3	59
#3	-23.365	924.0	1082.2	54
#4	-23.641	961.1	1040.5	56
#5	-22.645	751.7	1330.2	54
#6	-25.424	559.5	1787.4	63
#7	-24.219	1046.3	955.8	59
#8	-24.881	686.8	1456.1	62
#9	-24.220	825.5	1211.4	62
#10	-24.292	579.0	1727.2	61
	-24.06 $\pm$0.73	803 $\pm$152	1296 $\pm$268	

TABLE C.1

1ST ORDER MODELS: INFLUENCE OF SCAN SPEED, SOLID PLATE

V, mm/s	K, dB	τ, μs	ω_c, rad/s	fit, %	val, %
200	-16.203	307.0	3256.9	54	59
400	-17.059	673.1	1485.7	56	49
600	-19.005	473.6	2111.6	60	60
800	-20.575	459.6	2175.8	57	58
1000	-22.331	451.0	2217.1	60	54
1200	-23.720	414.4	2412.9	50	46
1400	-24.229	745.4	1341.5	43	42

TABLE C.2

1ST ORDER MODELS: INFLUENCE OF SCAN SPEED, DEEP POWDER

V, mm/s	K, dB	τ, μs	ω_c, rad/s	fit, %	val, %
200	-27.557	163.5	6116.2	36	28
400	-27.676	247.3	4043.7	47	44
600	-25.859	399.2	2504.8	54	52
800	-25.811	432.6	2311.6	53	42
1000	-25.871	398.5	2509.2	61	45
1200	-24.635	709.6	1409.2	56	57
1400	-24.994	560.5	1784.1	57	58

TABLE D

LAYER DEPENDENCE

	Layer	K, dB	τ, μs	ω_c, rad/s	fit, %
powder	1	-21.630	449.5	2224.8	43
	2	-23.685	629.6	1588.3	33
	5	-27.209	450.1	2221.5	61
	10	-28.267	359.6	2781.0	57
	20	-27.864	186.7	5356.6	33
	40	-28.730	166.1	6022.0	53
part	1	-21.975	249.3	4010.9	33
	2	-20.686	422.1	2368.9	38
	5	-23.769	522.6	1913.4	46
	10	-23.147	455.1	2197.3	61
	20	-23.842	440.2	2271.9	64
	40	-23.502	704.7	1419.0	57

REFERENCES

[1] ASTM International. ISO/ASTM52900-15 Standard Terminology for Additive Manufacturing - General Principles - Terminology. West Conshohocken, PA; ASTM International, 2015. doi: https://doi.org/10.1520/ISOASTM52900-15.

[2] M. Grasso and B. M. Colosimo, "Process defects and in situ monitoring methods in metal powder bed fusion: a review," *Meas. Sci. Technol.*, vol. 28, no. 4, p. 044005, 2017.

[3] G. Tapia and A. Elwany, "A review on process monitoring and control in metal-based additive manufacturing," *J. Manuf. Sci. Eng.*, vol. 136, no. 6, p. 060801, 2014.

[4] J. C. Heigel and B. M. Lane, "The effect of powder on cooling rate and melt pool length measurements using in-situ thermographic tecniques," *Solid Free. Fabr. Symp.*, Austin, TX, 2017.

[5] P. M. Sammons, M. L. Gegel, D. A. Bristow, and R. G. Landers, "Repetitive process control of additive manufacturing with application to Laser Metal Deposition," *IEEE Trans. Control Syst. Technol.*, vol. 27, no. 2, pp. 566575, Mar. 2019.

[6] T. Craeghs, F. Bechmann, S. Berumen, and J.-P. Kruth, "Feedback control of Layerwise Laser Melting using optical sensors," *Physics Procedia*, 2010, vol. 5, no. PART 2, pp. 505514.

[7] V. Renken, L. Lubbert, H. Blom, A. Von Freyberg, and A. Fischer, "Model assisted closed-loop control strategy for selective laser melting," *Procedia CIRP*, 2018, vol. 74, pp. 659663.

[8] A. Shkoruta, W. Caynoski, S. Mishra and S. Rock, "Iterative learning control for power profile shaping in selective laser melting," 2019 IEEE 15th International Conference on Automation Science and Engineering (CASE), Vancouver, BC, Canada, 2019, pp. 655-660.

[9] 4039 Development & demonstration of open-source protocols for powder bed fusion AM - America Makes. [Online]. Available: https://www.americamakes.us/portfolio/4039-development-demonstration-open-source-protocols-powder-bed-fusion-additive-manufacturing-pbfam/. [Accessed: 25-Sep-2019].

[10] B. Lane, S. Grantham, H. Yeung, and C. Zarobila, "Performance characterization of process monitoring sensors on the NIST Additive Manufacturing Metrology Testbed", *Solid Free. Fabr. Symp.*, Austin, TX, 2017.

[11] A. Gokhan Demir, C. De Giorgi, and B. Previtali, "Design and implementation of a multisensor coaxial monitoring system with correction strategies for Selective Laser Melting of a maraging steel", *J. Manuf. Sci. Eng.*, vol. 140, no. 4, p. 041003, Feb. 2018.

[12] A. Shkoruta, S. Mishra, and S. Rock, "Coaxial near-infrared camera measurements for process control in selective laser melting", *Proc. 34th ASPE Annual Meeting*, Pittsburgh, PA, 2019, pp. 54-59.

[13] M. J. B. Spector et al., "Passivity-based iterative learning control design for selective laser melting", *2018 Annual American Control Conference (ACC)*, Milwaukee, WI, 2018, pp. 5618-5625.